Pergamon

Int. J. Heat Mass Transfer. Vol. 38, No. 2, pp. 241–257, 1995
Copyright © 1994 Elsevier Science Ltd
Printed in Great Britain. All rights reserved
0017–9310/95 $9.50+0.00

0017–9310(94)00149–9

Numerical simulation of hot-dip metallic coating process

HUI ZHANG

Department of Mechanical Engineering, SUNY at Stony Brook, Stony Brook, NY 11794-2300, U.S.A.

and

M. KARIM MOALLEMI

Department of Mechanical Engineering, Polytechnic University, Brooklyn, NY 11201, U.S.A.

(*Received* 28 *February* 1994 *and in final form* 18 *May* 1994)

Abstract—The paper describes the modeling of the solidification process over a planar substrate which is being pulled through a melt bath at a constant speed. The complexities generated by the presence of the two moving/unknown boundaries are dealt with by solving the transient governing transport equations numerically, and by using an efficient finite volume scheme employing a multizone adaptive grid generating technique and a curvilinear finite volume approach. The temperature distributions in the solid and melt, the melt flow field in the bath, the thickness of the solidified layer, and the shape of the free surface are calculated and reported.

1. INTRODUCTION

During the last few decades, the hot-dip metallic coating technique has been utilized extensively in the manufacturing and cladding of wire, and the galvanizing and coating of metal strips, sheets, etc. [1, 2]. Recently, there has been renewed interest in this process for fabrication of tapers, lens-like waveguides, and mono- and multi-layer anti-reflection coatings of spatially varying thickness from colloids and supersaturated solutions [3, 4]. The modern applications of the dip-coating process, and the implementation of closed-loop computer controls in the traditional applications [5], require a fundamental understanding of the heat and mass transfer mechanisms involved in the deposition and/or solidification over a substrate that is pulled through and withdrawn from a finite bath.

In spite of the broad range of applications, the limited number of works on the problem are based on oversimplified models, and have neglected transport mechanisms which are particularly important in the modern applications. Seeniraj and Bose [6], for example, performed an analysis of freeze-coating of polymeric materials over a moving metallic substrate by assuming the temperature of the metallic object to remain constant and uniform, and the molten bath to be at its melting temperature. The first assumption is not appropriate for a substrate with finite thickness and heat capacity, while the second limits the analysis to the particular condition considered. Cheung [7] analyzed freeze coating on a flat plate where constant plate temperature and saturated liquid temperature conditions were relaxed. Whereas constant substrate temperature yielded a monotonic increase of coating thickness over the plate [6], finite heat capacity made it possible to predict initial deposition followed by remelting [7]. However, both of these studies cannot be rigorously used for analyzing dip-coating since they assume the existence of a leading edge for the solidification front as well as for the melt flow. In doing so the effects of bath geometry are ignored. Zhang *et al.* [8] conducted a numerical study of the dip-coating process in a finite-size bath, accounting for the buoyancy effects. They concluded that the boundary layer assumption for the melt flow over the moving solid is a gross simplification, particularly in the region near the bath floor, where the solidification rate is the highest. They had, however, neglected the axial heat conduction in the solid after leaving the bath, which defines the freezing rate during the final stage of contact between the solid and the melt. The capillary and thermocapillary effects were also neglected by assuming the free surface to be planar and adiabatic.

The axial heat conduction in the solid emerging out of the bath, and the capillary and thermocapillary effects, are of cardinal importance in the modern applications of the dip-coating process. In fabrication of waveguides by a microcontrolled dip coating process, the deposition takes place essentially in the meniscus, and is controlled by the withdrawal rate of the solution by the substrate and its heat transfer characteristics. In the traditional applications, recently, improvements in the coating characteristics have been achieved through utilization of "gas knife"

NOMENCLATURE

Ar	cavity aspect ratio $= H/D$
Bd	dynamic Bond number $= Ra/Ma$
Bo	static Bond number $= We/Fr$
c_p	specific heat
C	cavitation number $= (p_a - p_r)/\rho u_{si}^2$
d	plate thickness
D	half-width in the bath
F	performance function
Fr	Froude number $= u_{si}^2/gH$
g	gravitational acceleration
G	weight function of grid orthogonality
Gr	Grashof number $= g\beta H^3(T_h - T_f)/\nu_l^2$
h_{fs}	latent heat of fusion
H	melt height in the bath
I	grid characteristic
Ja	Jacobian of transformation $= x_\xi y_\eta - x_\eta y_\xi$
L	port height
M	inertial coefficient of the grid movement
Ma	Marangoni number $= (\partial\sigma/\partial T)(T_h - T_f)H/\mu\alpha$
p	pressure (isotropic stress component)
q	heat flux $= \partial\theta/\partial x^*$
Pr	Prandtl number $= \nu_l/\alpha$
R	radius of the curvature
Ra	Rayleigh number $= GrPr$
Re	Reynolds number $= u_{si}H/\nu_l$
Ste_l	liquid Stefan number $= c_{pl}(T_h - T_f)/h_{fs}$
Ste_s	solid Stefan number $= c_{ps}(T_f - T_{si})/h_{fs}$
t	time
T	temperature
u, v	velocity components in axial and radial directions
W	weight function of the volume or area
We	Weber number $= \rho u_{si}^2 H/\sigma$
x, y	coordinates.

Greek symbols

β	thermal expansion coefficient
γ	ratio of specific heats $= c_{ps}/c_{pl}$
δ	meniscus height
θ	dimensionless temperature
κ	ratio of thermal conductivities $= k_s/k_l$
ν	kinematic viscosity
ρ	mass density
σ	surface tension.

Subscripts

a	ambient
f	fusion
h	high temperature
i	inlet
int	interface
l	liquid
M	inertial
O	orthogonality
r	reference
s	solid
S	smoothness
t	top surface
W	weight
ξ, η	curvilinear coordinates.

technology [9, 10], that comprises high-pressure gas jets that impinge onto the moving plate above the meniscus. It deems feasible regulation of the coating thickness by controlling the "gas knife" parameters (i.e. the position and orientation of the knife with respect to the substrate surface and the fee surface, as well as gas temperature, pressure and velocity). The gas impingement, however, may influence more than one transport mechanism involved in the dip-coating process. Specifically, it may (a) change the axial cooling characteristic of the solid (b) reduce the height of the meniscus and melt withdrawal rate, and (c) affect the thermocapillary flow at free surface. Thorough understanding of the complex interaction of these effects is not available in the open literature, and is essential for efficient utilization of this technology.

The objective of this study is to examine how the cooling effect of the free surface and the solid at exit, and the surface tension involved in the dip-coating process interact to influence the solidification rate. The governing transport equations are solved numerically by using a multizone adaptive grid generating technique, along with a finite difference scheme developed for non-orthogonal control volumes. The free surface and solid/liquid interface equations have been developed carefully in the paper. The solidification process over a planar substrate which is being pulled at a constant speed through a melt bath is modeled.

2. FORMULATIONS

Hot-dip coating with jet finishing is a method of obtaining a coating of controlled weight and uniformity on hot-dip coated strip by passing the strip through an elongated jet of gaseous fluid as it leaves the molten pool [10]. A schematic representation of the process used in numerical simulation is shown in Fig. 1(a). The final solidified coating thickness is related to strip speed, jet nozzle operating parameters, coating metal and fluid properties, and surface tension. The complexities of this process are due to:

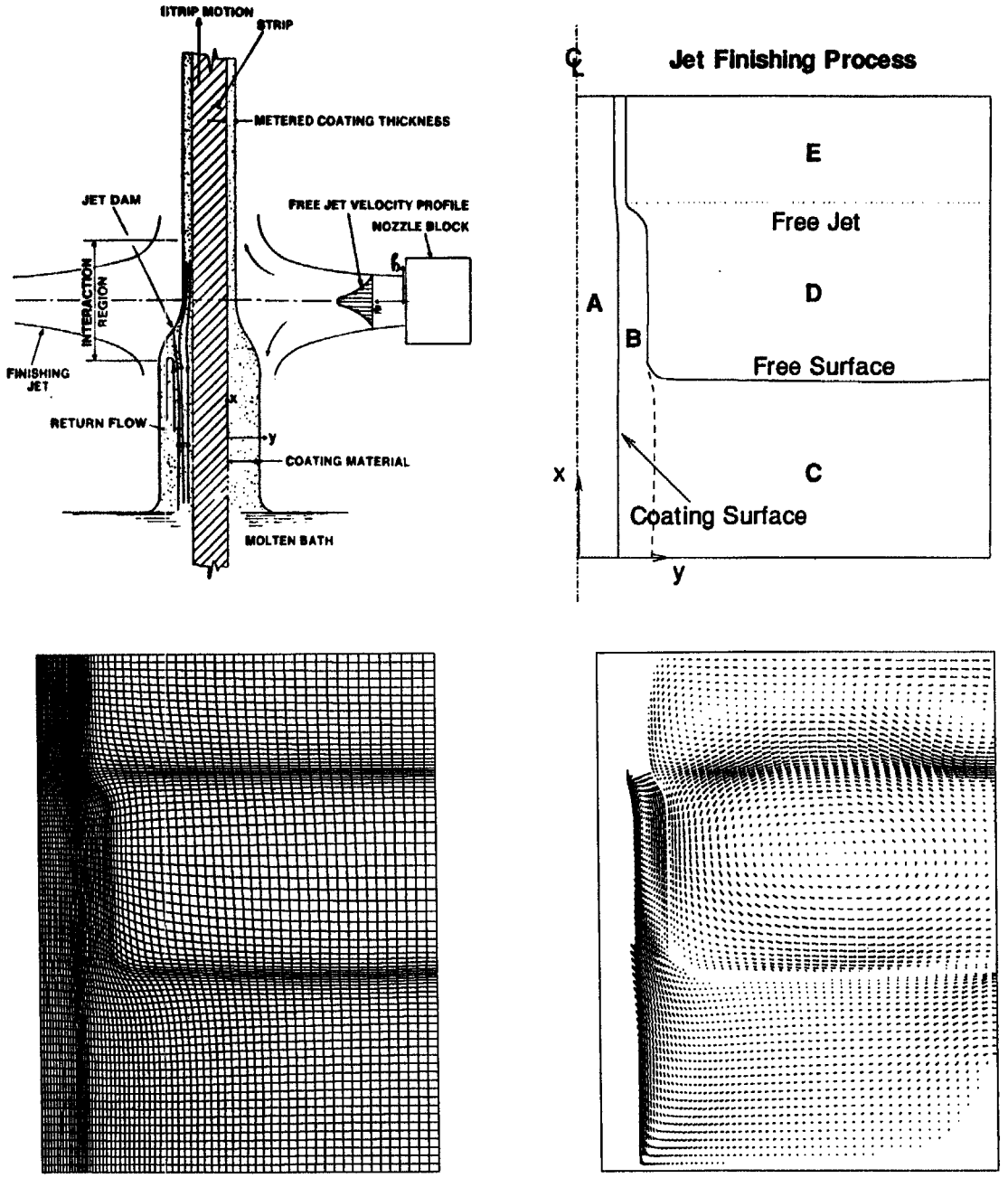

Fig. 1. (a) Schematic of the jet finishing process; (b) zone distribution; (c) grid distribution; (d) flow field distribution (liquid velocity has been enlarged 1000 times in the figure).

co-existence of three phases (solid, liquid and gas); irregular domain and two moving boundaries (the solid/liquid interface and the free surface); and a lot of sub-processes (gas jet system; strip moving system; molten coating material operating system) involved in the whole process systems. The zone and grid distributions have been investigated and the demonstration results are shown in Fig. 1(b)–(d). In Fig 1(d), the domain and interfaces are given: however, in the real calculation the shapes and locations are unknown and they are a part of the solution.

The case considered in this paper neglects the gas jet system: however, the cooling effect of the gas jet is considered from the boundary conditions. A dip-coating system which is considered in the modeling is schematically depicted in Fig. 2, where the gas phase is not included. A metal flat plate of thickness d_{si} is pulled at speed u_{si} through a molten metal bath of height H. The plate enters the bath at a temperature below the fusion temperature, $T_{si} < T_f$, and a crust solidifies over its surface that may grow or remelt as the plate moves vertically in the bath. Liquid at $T_{li} > T_f$

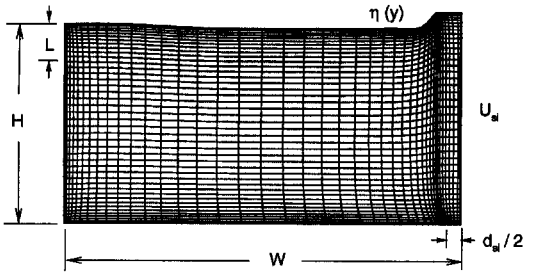

Fig. 2. Schematic diagram of the hot-dip coating system.

is introduced to the bath to compensate for the mass removed via solidification, so that the bath height remains constant during a simulation. To formulate the problem, the following simplifying assumptions are used: (1) laminar flow; (2) Newtonian phase behavior; (3) local thermodynamic equilibrium; (4) constant properties with the exception of the density in the buoyancy term (Boussinesq approximation); and (5) the moving plate and the solidified layer are of the same material [11].

The governing equations are non-dimensionalized using the following dimensionless variables:

$$(x^*, y^*) = (x, y)/H \quad t^* = tu_{si}/H \quad (u^*, v^*) = (u, v)/u_{si}$$

$$p^* = (p - p_r)/(\rho u_{si}^2) \quad \theta = (T - T_f)/(T_{li} - T_f).$$

With above assumptions and dimensionless variables, the problem is governed by conservation equations for mass, momentum and energy in the liquid melt, and the energy equation in the solid to yield:

continuity

$$\nabla \cdot \mathbf{U}^* = 0 \tag{1}$$

X-momentum

$$\frac{\partial u^*}{\partial t^*} + \nabla \cdot (\mathbf{U}^* u^*) = \nabla \cdot \left(\frac{1}{Re} \nabla u^* \right) - \frac{\partial P^*}{\partial x^*} + \frac{Gr}{Re^2} \theta_l \tag{2}$$

Y-momentum

$$\frac{\partial v^*}{\partial t^*} + \nabla \cdot (\mathbf{U}^* v^*) = \nabla \cdot \left(\frac{1}{Re} \nabla v^* \right) - \frac{\partial P^*}{\partial y^*} - \frac{1}{Fr} \frac{\partial \eta^*}{\partial y^*} \tag{3}$$

energy in liquid

$$\frac{\partial \theta_l}{\partial t^*} + \nabla \cdot (\mathbf{U}^* \theta_l) = \nabla \cdot \left(\frac{1}{RePr} \nabla \theta_l \right) \tag{4}$$

energy in solid

$$\frac{\partial \theta_s}{\partial t^*} + \nabla \cdot (\mathbf{U}_s^* \theta_s) = \nabla \cdot \left(\frac{\kappa/\gamma}{RePr} \nabla \theta_s \right). \tag{5}$$

In the above equations, $\mathbf{U}$ is the melt velocity vector with u and v components in x and y directions, respectively, and κ and γ are thermal conductivity ratio and specific heat ratio between solid and liquid, respectively. In equation (3), the last term on the right hand side comes from the definition of the pressure:

$$P^* = p^* + \frac{1}{Fr}(1 + \delta^* - x^*) \tag{6}$$

where $\delta = \delta(t^*, y^*)$ is the meniscus height.

For the boundary conditions, no-slip and adiabatic conditions are used over the bottom surface and wall of the bath. At the initiation of the numerical simulation, a fresh planar solid is introduced into the bath with a constant vertical velocity $u_{si}^* = 1.0$ and a uniform temperature $\theta_{si} = -Ste_s/\gamma Ste_l$. The average height of the melt bath H is kept constant during a simulation by compensation for the melt removed from the bath via solidification on the planar solid. Liquid phase-change material, at $\theta_{li} = 1.0$, is introduced into the bath from a port on its wall with a constant velocity, which is calculated by total liquid material mass balance, and the height of the port L is adjusted in different simulations such that the velocity of melt entering the bath is not greater than 10% of the solid velocity.

Solidification of a pure substance with a definite fusion temperature T_f is modeled: therefore, the solid and liquid phases are separated by a sharp interface, $F(x^*, y^*, t^*) = 0$, at which the temperature is required to be continuous,

$$\theta_s(x^*, y^*, t^*) = \theta_l(x^*, y^*, t^*) = 0. \tag{7}$$

The energy balance at the solid/liquid interface defines its position and motion can be derived as [12]

$$\rho_s h_{fs} (\mathbf{U}_{int} + \mathbf{U}_{si}) \cdot \mathbf{n} = k_s \frac{\partial T_s}{\partial n} - k_l \frac{\partial T_l}{\partial n} \tag{8}$$

where densities of the two phases are assumed equal, $\mathbf{U}_{si}$ is the plate velocity and $\mathbf{U}_{int} \cdot \mathbf{n}$ is the interface normal velocity which can be calculated as follows:

$$\mathbf{U}_{int} \cdot \mathbf{n} = \frac{\mathbf{U}_{int} \cdot \nabla F}{|F|} = -\frac{\partial F / \partial t}{|F|}. \tag{9}$$

Combining above two equations, the dimensionless form of the equation can be written as follows:

$$\frac{\partial F}{\partial t^*} = [\mathbf{U}_{si}^* + \frac{Ste_l}{Re \cdot Pr} (\nabla \theta_l - \kappa \nabla \theta_s)] \cdot \nabla F. \tag{10}$$

At the free surface, the required hydrodynamic conditions are: (1) the fluid particles at the surface must remain attached (kinematic condition); (2) the surface tension is a function of temperature only; (3) the tangential shear stress is due to the variation of surface tension of the liquid (shear stress in the gas on the other side of the free surface is neglected); and (4) the liquid and the atmospheric pressure must be balanced, except for surface tension effects [13]. Denoting the free surface position by $x_f^* = 1 + \delta^*(t^*, y^*)$, the above conditions have the following dimensionless forms:

$$u^* = \frac{D\delta^*}{Dt^*} = \frac{\partial \delta^*}{\partial t^*} + v^* \frac{\partial \delta^*}{\partial y^*}, \tag{11}$$

Table 1. Governing parameters and baseline data

Parameter	Definition	Values used
Cavity aspect ratio	$Ar = H/D$	0.5
Conductivity ratio	$\kappa = k_s/k_l$	2.5
Specific heat ratio	$\gamma = c_{ps}/c_{pl}$	1.0
Cavitation number	$C = (p_a - p_v)/\rho u_{si}^2$	0.0
Rayleigh number	$Ra = g\beta H^3(T_{li} - T_f)/\nu_l\alpha_l$	1000
Reynolds number	$Re = U_s H/\nu_l$	666.7
Prandtl number	$Pr = \nu_l/\alpha_l$	0.015
Solid Stefan number	$Ste_s = c_{ps}(T_{si} - T_f)/h_{fs}$	0.0545
Liquid Stefan number	$Ste_l = c_{pl}(T_{li} - T_f)/h_{fs}$	0.0273
Froude number	$Fr = u_{si}^2/gH$	0.1 or 0.0
Weber number	$We = \rho u_{si}^2 H/\sigma$	inf
Marangoni number	$Ma = (d\sigma/dT)(T_{li} - T_f)H/\mu\alpha$	0.0
Dynamic contact angle		$\pi/2$
Solid Nusselt number	$\{\partial\theta/\partial n^*\}_{x^* = 1+\eta^*}$	0.0
Liquid Nusselt number	$\{\partial\theta/\partial x^*\}_{x^* = x_f^*}$	0.0

$$\frac{\partial v^*}{\partial x^*} = \frac{Ma}{RePr}\frac{\partial \theta_l}{\partial y^*} \tag{12}$$

$$p^* = C - \frac{1}{We}\left(\frac{1}{R^*}\right) \tag{13}$$

where Ma, We and C are Marangoni number, Weber number and cavitation number, and R^* is the dimensionless radius of curvature of the surface given by

$$\frac{1}{R^*} = \frac{\partial^2\delta^*/\partial y^{*2}}{[1 + (\partial\delta^*/\partial y^*)^2]^{3/2}}. \tag{14}$$

To examine the effects of "gas knife", heat loss is introduced at the free surface on the melt flow in the bath: adiabatic or convective and radiation cooling conditions were simulated, i.e.

$$\left\{\frac{\partial\theta_l}{\partial n}\right\}_{x^* = 1+\delta^*} = q_l. \tag{15}$$

Adiabatic or conductive cooling conditions were used for the solid emerging from the bath:

$$\left\{\frac{\partial\theta_s}{\partial x^*}\right\}_{x^* = x_f^*} = q_s. \tag{16}$$

The governing equations (1)–(5) indicate that the problem is characterized by dimensionless numbers Re, Gr, Pr, Fr, We, q_s, and q_l which are defined in Table 1. The ratio of the thermal conductivities κ, ratio of heat specifics γ, aspect ratio Ar, contact angle, Stefan number of liquid, Stefan number of solid, Marangoni number, and cavitation number are also defined in Table 1.

3. SOLUTION PROCEDURE

The principal difficulties in the analysis of multidimensional phase-change problems arise from the fact that the position of the solid/liquid interface is not known *a priori* and is not necessarily along the coordinate contours. Numerous methodologies have been developed to predict phase-change in the presence of melt flow due to buoyancy or other forces. In this study, additional complications are introduced by the presence of the free surface that is not planar and is also part of the solution.

To overcome the difficulties associated with the timewise changing domains and irregular boundaries, the Multizone Adaptive Grid Generation (MAGG) technique and the Curvilinear Finite Volume (CFV) approach [14, 15] were employed. The detail descriptions can be seen in refs. [14, 15]. In this paper, overviews of the MAGG and CFV approach are provided, and important features of the numerical solution procedure are highlighted.

The MAGG technique is desirable in situations where the problem domain is composed of regions with vastly different physical properties and/or internal moving boundaries. Under these circumstances, the grid system will be generated for different zones present, such that internal boundaries separating these zones coincide with some grid lines. With this feature, while the grid nodes in different zones are allowed to move (in response to the development of the solution, movement of the external boundaries or the internal boundaries themselves), the interfaces between the zones are preserved and grid points are only permitted to move along them [14, 15]. Zhang and Moallemi have developed two-dimensional formulations by using the variational method to minimize a linear combination of integrals which are measures of different grid characteristics; namely, the smoothness I_S, orthogonality I_O, weighted cell area I_W, and inertia I_M of the grids. These integrals may be written as [15–20]

$$I_S = \iint\left(\frac{x_\xi^2 + x_\eta^2 + y_\xi^2 + y_\eta^2}{Ja}\right)d\xi\, d\eta \tag{17}$$

$$I_O = \iint G(x_\xi x_\eta + y_\xi y_\eta)^2\, d\xi\, d\eta \tag{18}$$

$$I_W = \iint W Ja^2\, d\xi\, d\eta \tag{19}$$

$$I_M = \int\int M(\xi,\eta)\,(\mathbf{x}-\mathbf{xO})^2\,d\xi\,d\eta \qquad (20)$$

where W and G are weight functions which are to be specified to control grid volume (area) and orthogonality, respectively, $M(\xi,\eta)$ is the inertia coefficient, **xO** is a given mesh, for example, the mesh of the last time-step, and Ja is the Jacobian of the mapping,

$$Ja = x_\xi y_\eta - x_\eta y_\xi \qquad (21)$$

with subscripts denoting the variables with respect to which partial differentiation is performed.

A grid generator may be made part of an algorithm to adapt the grid distribution to data generated by the solution of the finite difference equations, by using an appropriate weight function $W(x,y)$ (e.g. some measure of the solution variation or error), resulting in a finer grid where the weight is large. The choices of the weighting functions W and G are generally problem dependent. The grid generation system is formed by minimizing a weighted sum of integrals (17)–(20),

$$I = I_S + \lambda_O I_O + \lambda_W I_W + \lambda_M I_M = \int\int F\,d\xi\,d\eta \qquad (22)$$

where F is the kernel of the functional, which is also referred to as the overall "performance function" of the optimization problem [21]. The Euler's equations for the variational problem (22) form a system of partial differential equations from which the coordinates of the grid nodes are calculated,

$$\left(\frac{\partial}{\partial x} - \frac{\partial}{\partial \xi}\frac{\partial}{\partial x_\xi} - \frac{\partial}{\partial \eta}\frac{\partial}{\partial x_\eta}\right)F = 0$$

$$\left(\frac{\partial}{\partial y} - \frac{\partial}{\partial \xi}\frac{\partial}{\partial y_\xi} - \frac{\partial}{\partial \eta}\frac{\partial}{\partial y_\eta}\right)F = 0. \qquad (23)$$

This grid generation routine is formulated via the variational problem (22) for the entire domain, with the exception of the zonal interfaces along which the grid distribution is obtained by the same two-dimensional variational problem, subject to constraints of the form

$$g_I \triangleq g_I(x,y) = 0, \quad \text{for } I = I_1, \quad I = I_2, \ldots$$
$$\text{with} \quad I_{\min} < I_i < I_{\max} \qquad (24)$$

where g_Is are known real-valued functions with respect to arguments x and y, which are implicit functions of ξ and η, and define the interfaces for constant η_I values. The above constrained optimization problems are converted to unconstrained ones by introducing Lagrange multipliers Λ_I [21] to form augmented functionals:

$$I = \int\int (F + \Lambda_I g_I)\,d\xi\,d\eta. \qquad (25)$$

The Euler–Lagrange equations of the above expression along with the constraint (24) provide the necessary conditions for finding the grid distribution $(x(\xi,\eta_I), y(\xi,\eta_I))$ and the Lagrange multiplier Λ_I. The interface position function and its derivatives are determined from an accurate curving fitting procedure [22] in order to preserve its shape, while the grid points move along it.

The multizone adaptive grid generation technique used here, explained in more detail in ref. [15], is more efficient and has better characteristics than previous ones [11, 18, 19]. This is mainly due to the direct and dynamic link between the zonal and interfacial grid generation routines that is provided by the presence of second-order derivatives (e.g. $x_{\eta\eta}$ and $y_{\eta\eta}$) in this formulation. The finite difference approximation of the Euler's equations are formed and solved by the SOR method to determine the coordinates of the grid points [15].

The curvilinear finite volume approach is based on flux discretization in the physical domain and, therefore, modifications in the physical process models may be easily implemented, and the predictions may be readily examined. The governing equations of the transport processes, controlled by diffusion and convection, can be cast into a general form as

$$\frac{\partial r^n \rho\phi}{\partial t} + \nabla\cdot(r^n \rho \mathbf{u}\phi) = \nabla\cdot(r^n \Gamma \nabla\phi) + r^n S \qquad (26)$$

where the geometry index n has a value of 0 for planar and 1 for the axisymmetric coordinate systems, ϕ is the general dependent variable, S is the volumetric source of ϕ, ρ is mass density, **u** is the velocity vector, and Γ is the diffusion coefficient for ϕ. The above equation can be written in a generalized coordinate system (ξ,η) as follows [23, 24]:

$$\frac{\partial}{\partial t}(r^n Ja\,\rho\phi) + \frac{\partial}{\partial \xi}\left(\rho U\phi - \frac{\alpha_\xi \Gamma}{h_\xi}\frac{\partial\phi}{\partial\xi}\right) + \frac{\partial}{\partial \eta}\left(\rho V\phi - \frac{\alpha_\eta \Gamma}{h_\eta}\frac{\partial\phi}{\partial\eta}\right) = r^n Ja\,S(\xi,\eta) - \frac{\partial}{\partial\xi}\left(\frac{\beta_\xi\Gamma}{h_\eta}\frac{\partial\phi}{\partial\eta}\right) - \frac{\partial}{\partial\eta}\left(\frac{\beta_\eta\Gamma}{h_\xi}\frac{\partial\phi}{\partial\xi}\right) \qquad (27)$$

where h_ξ, h_η, α_ξ, β_ξ, α_η, and β_η are geometric coefficients [24]. In above general equation, U and V are the relative contravariant velocity components normal to the constant ξ- and η-coordinate lines, respectively. These are related to the covariant velocity components (u_ξ, u_η) and the grid velocity components (u_g, v_g) through

$$U = \alpha_\xi u_\xi - \beta_\xi u_\eta - r^n u_g \quad V = \alpha_\eta u_\eta - \beta_\eta u_\xi - r^n v_g. \qquad (28)$$

The grid velocity components are defined as

$$u_g = \frac{\partial y}{\partial\eta}\frac{\partial x}{\partial t} - \frac{\partial x}{\partial\eta}\frac{\partial y}{\partial t} \quad v_g = \frac{\partial x}{\partial\xi}\frac{\partial y}{\partial t} - \frac{\partial y}{\partial\xi}\frac{\partial x}{\partial t}. \qquad (29)$$

The merits of this methodology have been demonstrated through its successful application to the simulation of different flow and heat transfer prob-

lems in complex geometries, and transport processes involving free and moving boundaries [15].

The governing equations for the liquid phase, equations (1)–(4), and the solid, equation (5), were solved iteratively and independently by invoking the quasi-steady-state assumption for the solid/liquid interface. At the free surface, equations (9) and (10) were used as boundary conditions for x- and y-momentum equations, respectively; and equations (11), (12) were used along with the pressure equation to adjust the height of the free surface after each iteration for a given time step. With the interface fixed at any time step, the fusion temperature at the interface, equation (7), was enforced as the boundary condition for both phases. At any time step, after the solutions for the two regions were converged to the desired accuracy, the interface energy balance equation (8) was employed to evaluate the new position of the solidification front along the plate.

After conducting a few grid sensitivity runs and in a compromise between accuracy and computational time, a grid system containing 32×42 nodal points in the melt, and 10×42 nodal points in the solid was used.

Automatic time step control is incorporated in the program, based on the maximum local interface displacement being less than 10% of the local grid width, to avoid numerical oscillation at early times into the simulation, which may happen if the displacement is greater than 50% of the local grid width. At any time step the solution was considered converged if

$$\frac{|\psi^{n+1}(i,j)-\psi^{n}(i,j)|}{\mathrm{Max}|\psi^{n+1}(i,j)|} < 10^{-4} \qquad (30)$$

where i and j refer to computational nodes, n is the iteration loop counter and ψ is u, v, θ_l, and θ_s. The residual source of mass was less than 10^{-12} for all the cases examined.

4. RESULTS AND DISCUSSION

The problem is a steady-state one (with respect to a coordinate system fixed to the bath), but it is cast in time-dependent form for convenience in the numerical implementation. The initial conditions are arbitrary and are taken to be such that the melt is at rest and at the fusion temperature of the phase-change material. At the initiation of the numerical simulation, a planar solid of thickness d_{si}^* enters the bath with a constant vertical velocity u_{si}^* and a uniform temperature θ_{si}. The height of the melt at the inlet of the bath is kept constant during a simulation by introducing liquid phase-change material at θ_{li}, into the bath with a uniform velocity U_{li}^*, which is evaluated at each time step by comparing the solid mass entering the bath with the solid mass exiting the bath.

The flow and heat transfer in the melt and the thickness of the solidified layer are governed by 15 independent dimensionless parameters, listed in Table 1. The large number of the independent parameters prohibit a complete parametric study of the problem. The intent here is to demonstrate the applicability of the methodology developed in this paper to a rather complex phase-change problem. The cases discussed here, however, will illustrate: (1) superheating effect of the melt; (2) subcooling effect and pull rate of the solid substrate entering the bath; (3) the influence of capillary and thermocapillary on the shape of the free surface; and (4) the influence of cooling of the solid at exit and the free surface on the fluid flow and the thickness of the solidified layer. The baseline case, shown in Table 1, serves as a reference for comparison with the results of variations of the various dimensionless parameters. In Table 1, the values of $Ste_s = 0.0545$ and $Ste_l = 0.0273$ correspond to 20°C subcooling of the solid and 10°C superheating of the melt of aluminum, respectively. The free surface and the solid emerging from the bath are taken to be adiabatic, and other parameters, $Fr = 0.1$, $We = \infty$, $Ma = 0$, and $\phi = \pi/2$, are used.

Figure 3(a) and (b) presents the flow field and temperature distribution in the bath for the baseline conditions, corresponding to $Gr/Re^2Ar = 0.3$. The right boundary of the graphs is the centerline of the moving solid substrate when melt is introduced from the port in the wall. The streamlines corresponding to the inlet flow terminate at the solid/liquid interface (illustrating mass continuity) as all the mass entering is eventually solidified on the plate. The flow field established is mainly due to the shear induced by the solid motion, with a minor contribution from thermal buoyancy. The buoyancy-induced flow opposes the plate shear induced flow. The shear induced recirculation diverts the hotter melt entering the bath towards the left bottom corner adiabatic surface where a small secondary eddy is formed. The surface tension force is causing the formation of the meniscus which, in the absence of the Marangoni effect, helps the smooth diversion of the boundary layer flow. The temperature distribution in the bath is in agreement with the flow field and indicates a weak buoyancy. The solid temperature changes very abruptly as it enters the bath and is exposed to the melt.

Figures 4 and 5 present the flow fields and temperature distributions in the bath for $Ra = 3333.3$, and $Ra = 10\,000$, corresponding to $Gr/Re^2Ar = 1.0$, 3.0, respectively. All other parameters remain at their baseline values. It is seen that the flow field established is due to an interaction between the buoyancy in the melt and the shear induced by the solid motion. By increasing the contribution of buoyancy, i.e. increasing the Rayleigh number, the larger natural convection cell is enlarged, as shown in Figs. 3(a), 4(a) and 5(a), and the temperature distributions in the bath also indicate stronger buoyancy, as shown in Figs. 3(b), 4(b), and 5(b). The equal contributions of buoyancy and shear to the melt flow are observed in Fig. 4, corresponding to $Gr/Re^2Ar = 1.0$.

The effects of Stefan numbers Ste_l and Ste_s on the

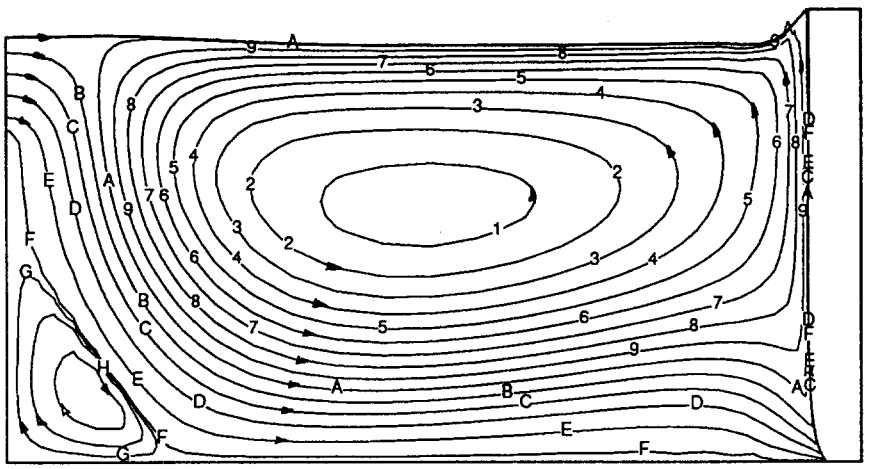

Level	st
I	0.0033
H	0.0011
G	0.0001
F	-0.0005
E	-0.0084
D	-0.0223
C	-0.0363
B	-0.0503
A	-0.0643
9	-0.0782
8	-0.0922
7	-0.1062
6	-0.1201
5	-0.1341
4	-0.1481
3	-0.1621
2	-0.1760
1	-0.1900

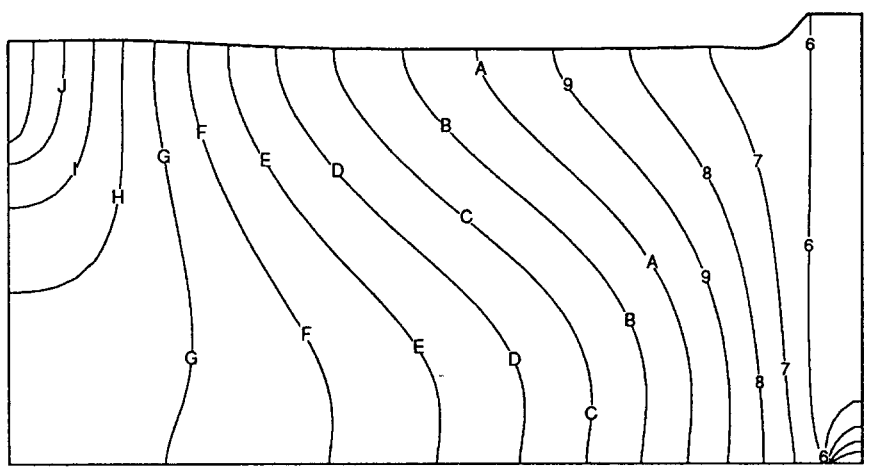

Level	t
K	0.9500
J	0.8821
I	0.8143
H	0.7464
G	0.6786
F	0.6107
E	0.5429
D	0.4750
C	0.4071
B	0.3393
A	0.2714
9	0.2036
8	0.1357
7	0.0679
6	0.0000
5	0.0000
4	-0.3735
3	-0.7469
2	-1.1204
1	-1.4938

Fig. 3. Stream function distribution in the bath, and temperature contours in the solid and the melt, $Gr/Re^2Ar = 0.3$.

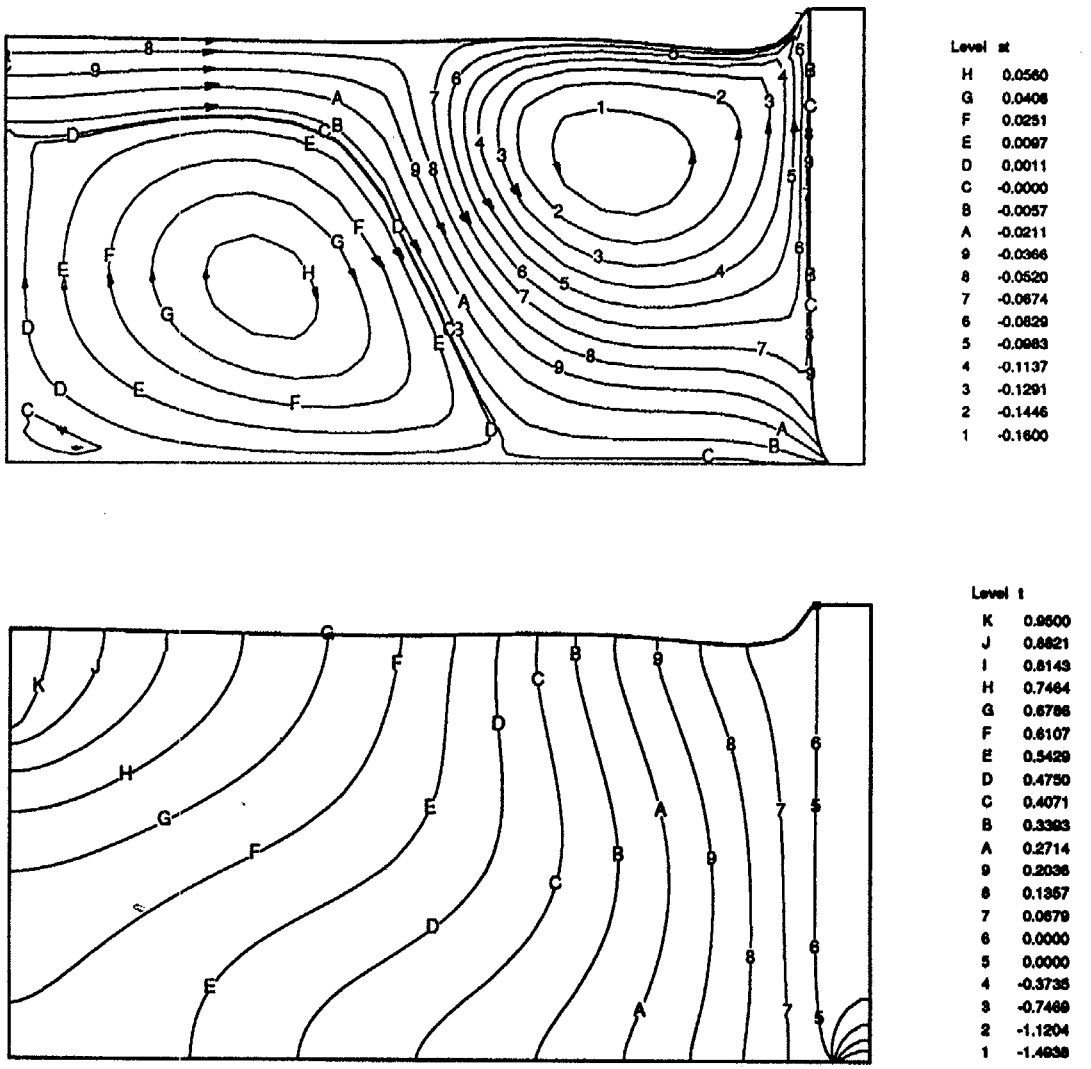

Fig. 4. Stream function distribution in the bath, and temperature contours in the solid and the melt, $Gr/Re^2Ar = 1.0$.

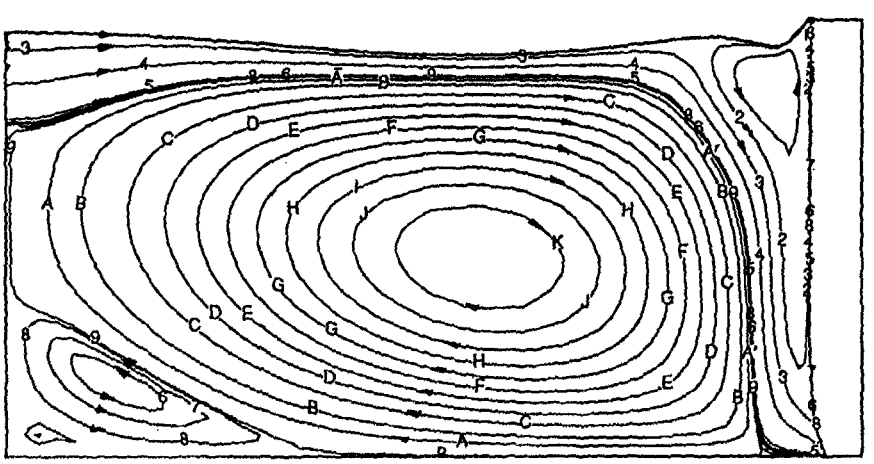

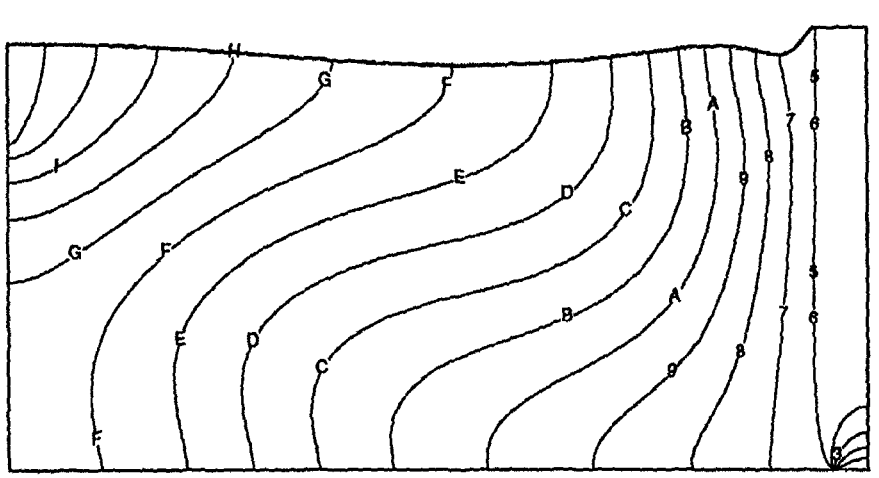

Fig. 5. Stream function distribution in the bath, and temperature contours in the solid and the melt, $Gr/Re^2Ar = 3.0$.

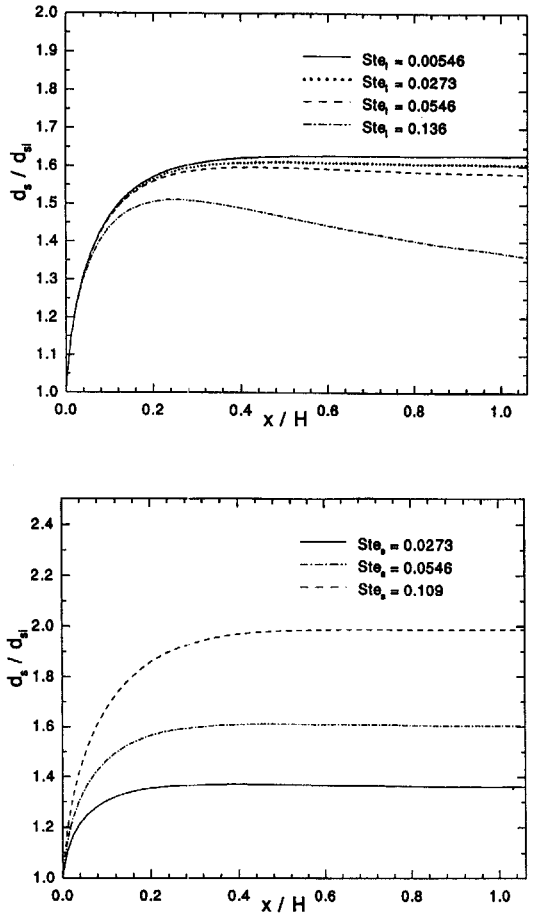

Fig. 6. (a) Effect of liquid Stefan number on solidification thickness; (b) effect of solid Stefan number on solidification thickness.

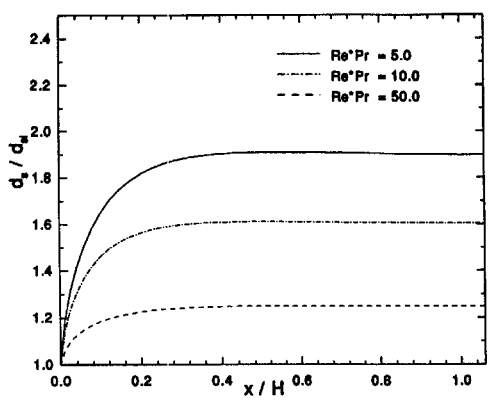

Fig. 7. Effect of Reynolds number on solidification thickness.

thickness of the solidified layer are presented in Fig. 6(a) and (b). The values of Ste_l and Ste_s used in the simulations are shown in the figure, and the other parameters keep their baseline values. The Stefan number of the liquid is a measure of superheating level of the melt: therefore, the thickness decreases with the increase of Ste_l, as expected, in Fig. 6(a). The growth of the solidified layer is defined by the energy balance at the interface, and the remelting of the solidified layer may occur if the superheating is strong enough to overcome the subcooling effect in the solid substrate, as shown in Fig. 6(a). The solid Stefan number indicates the level of the subcooling; its decrease reduces the solidification rate as shown in Fig. 6(b).

The effect of the Reynolds number on the coating thickness is illustrated in Fig. 7. Reducing the Reynolds number leads to an increase of the residence time of the solid substrate in the melt, which results in more solidification and a larger exit thickness. However, since the sensible heat of the solid substrate is limited by its inlet temperature, the increasing of the residence time may not lead to an appreciable increase in the solidification after a certain limit. The value of this limit is mainly a function of the solid and liquid Stefan numbers and the thermal properties. When the residence time exceeds the above limit, the solid substrate will start to remelt even at small levels of Ste_l.

In the range of parameters examined, the influence of the capillary force is found to be limited in the region near the free surface. The variations of the shape and location of the free surface due to changing Fr and We are shown in Fig. 8(a) and (b). Free surface shapes are wavy, and correspond to the flow fields presented in Figs. 3–5. The Weber number is set to infinity for two cases shown in Fig. 8(a), i.e. surface tensions are set to zero. By comparing Fig. 8(a) and (b), the Froude number is observed to be an important rate in defining the meniscus height. The thickness of the solidified layer, however, is hardly affected by the changes of the meniscus height. This is essentially due to the fact that the free surface shape does not cause a significant change in the flow field, and, at the same time, the solid temperature is very close to the fusion temperature, owing to adiabatic boundary conditions assumed for the solid exiting the bath. It is also found that the shape of the free surface becomes smooth (more planar) when the surface tension is present, while the Weber number has little effect on the meniscus height for the conditions examined. The thermocapillary force, however, is found to affect the solidification thickness by altering the flow field near the free surface. Figure 9 shows the growth of the deposited layer in the bath for different values of Ma. For positive values of Ma, the surface shear pulls the melt away from the solid, causing the melt boundary layer over the solid to thicken near the free surface. This yields a slightly high solidification rate. However, for negative values of Ma, the melt is pushed towards the solid by the free surface shear, creating a small circulation zone in the meniscus region, which causes some remelting of the solid. It is worth mentioning that, while most pure metals have positive Marangoni numbers, impurities tend to change the sign of $d\sigma/dT$, giving rise to flow of melt towards the moving solid, and some remelting of the solidified layer.

The influence of heat losses at the free surface, and through the solid, on the thickness of the solidified layer is shown in Fig. 11. q_l is the natural convection

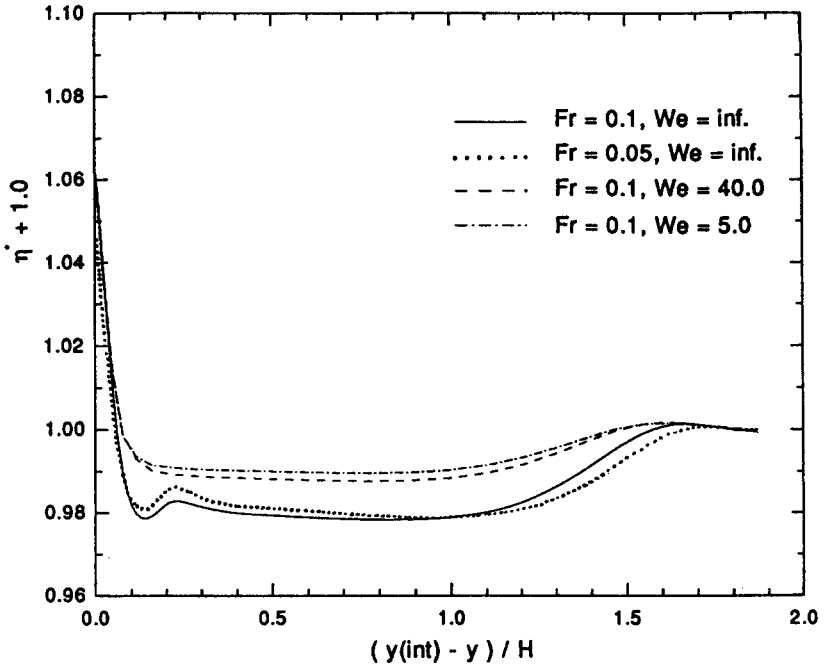

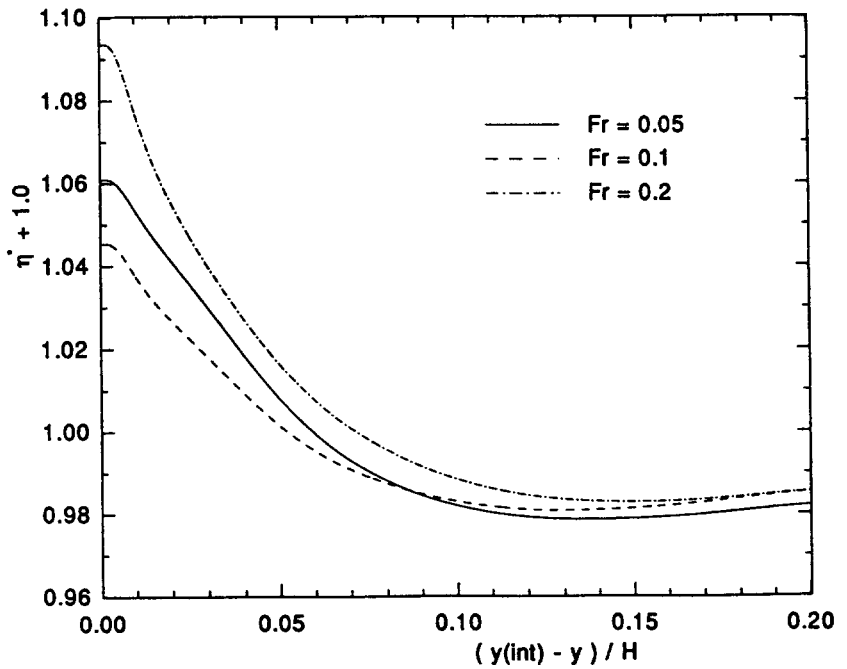

Fig. 8. Effects of Froude and Weber number on the meniscus profile.

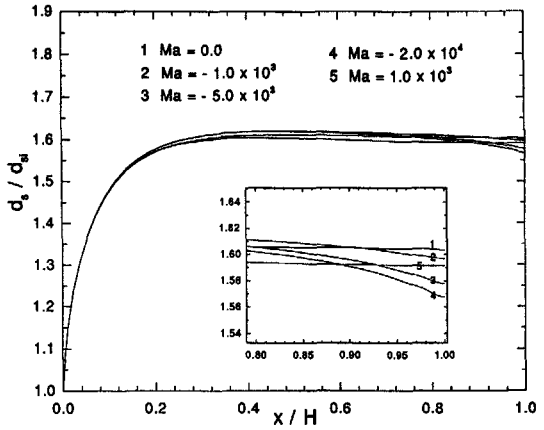

Fig. 9. Effect of Marangoni number on solidification thickness.

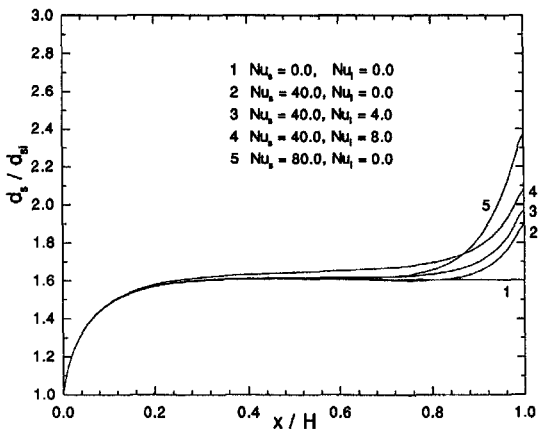

Fig. 10. Effects of heat losses through solid and free surface on solidification thickness.

cooling of the free surface by the ambient air or forced convection cooling due to "gas knife" flow. The natural convection cooling on the free surface is imposed only on the right half of the free surface, the other part of the free surface is kept adiabatic. The results illustrate that the solidification rates are generally higher with cooling of the free surface or the solid. Overall, the cooling of the solid has a more pronounced effect on the solidification than cooling of the melt. The melt cooling changes the flow pattern in the bath and, thus, has an indirect effect on the solidification process; whereas the cooling of the solid upon emergence from the bath directly influences the solidification rate.

Figures 11–13 show the effect of surface heat loss on the flow fields and temperature distributions for $Fr = 0$. When comparing Fig. 11 with Fig. 13, it is noted that the flow patterns are quite different. The explanation is that the cooling of the solid at the exit has changed the temperature gradient in this area. In view of the local energy balance, the liquid temperature distribution should vary with the cooling factor at the exit. Thus the flow pattern in Fig. 13 is expected to be different from the one in Fig. 11. In Figs. 11 and 13, the temperature of the melt remains above the melting point, but in Fig. 12 the temperature drops below the melting point. When the subcooling temperature of the melt reaches a critical value, the liquid may suddenly solidify and possibly move towards the solidified layer due to the surface tension and buoyancy force in the free surface. Furthermore, it may attach to the solidified layer and destroy the dip-coating process.

5. CONCLUSIONS

Numerical computations have been performed for the hot-dip metallic coating processes. The governing transport equations are solved numerically by using the MAGG technique and curvilinear finite volume approach. By using a weighting function in the grid generating routine, the grid points are forced to remain clustered near the interface where the temperature gradients are largest. Capillary and thermocapillary forces are observed to play a significant role in defining the shape of the free surface. The flow structure in the bath, however, is determined by the interaction between the shear induced by the moving

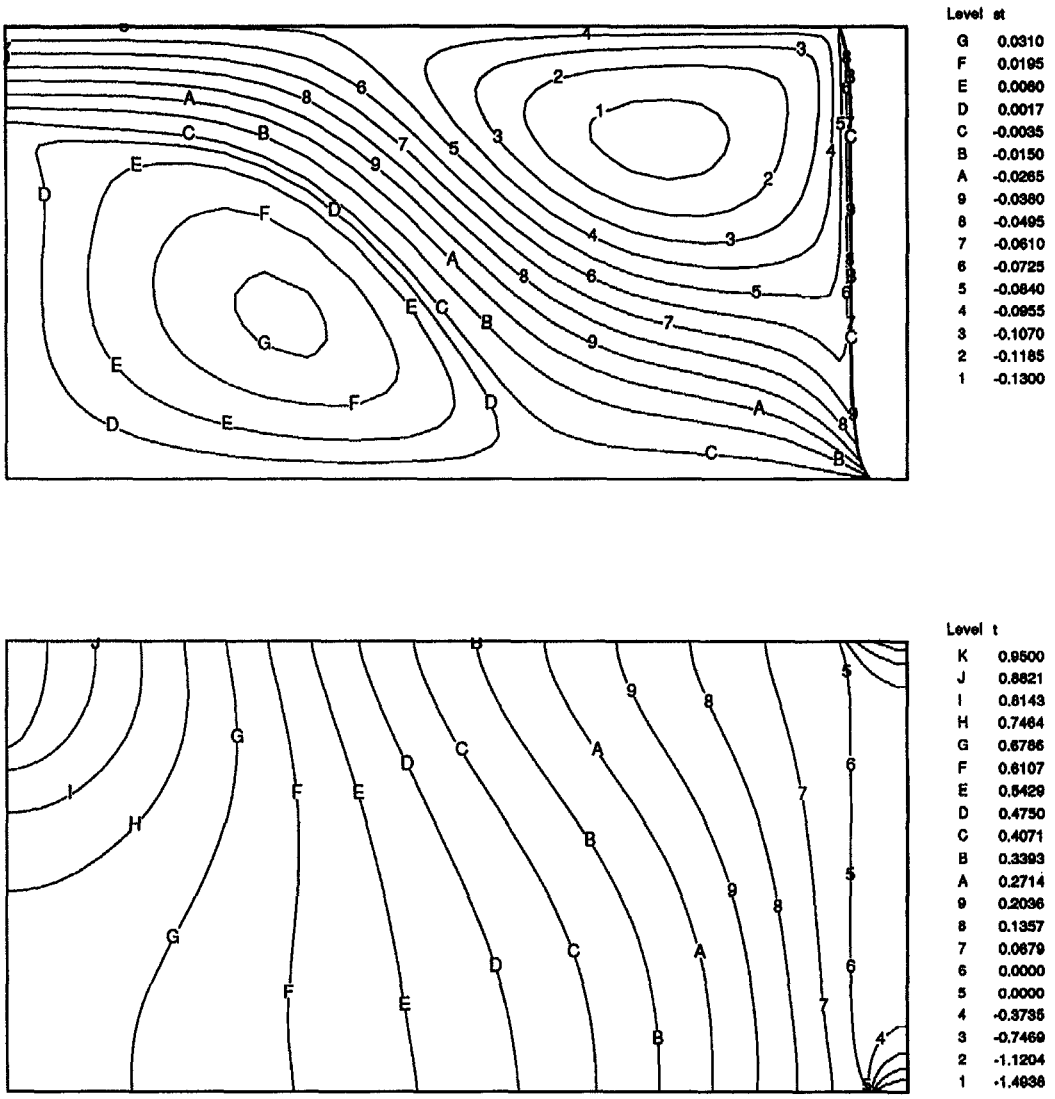

Fig. 11. Stream function distribution in the bath, and temperature contours in the solid and the melt, $q_s = 40$, $q_l = 0$.

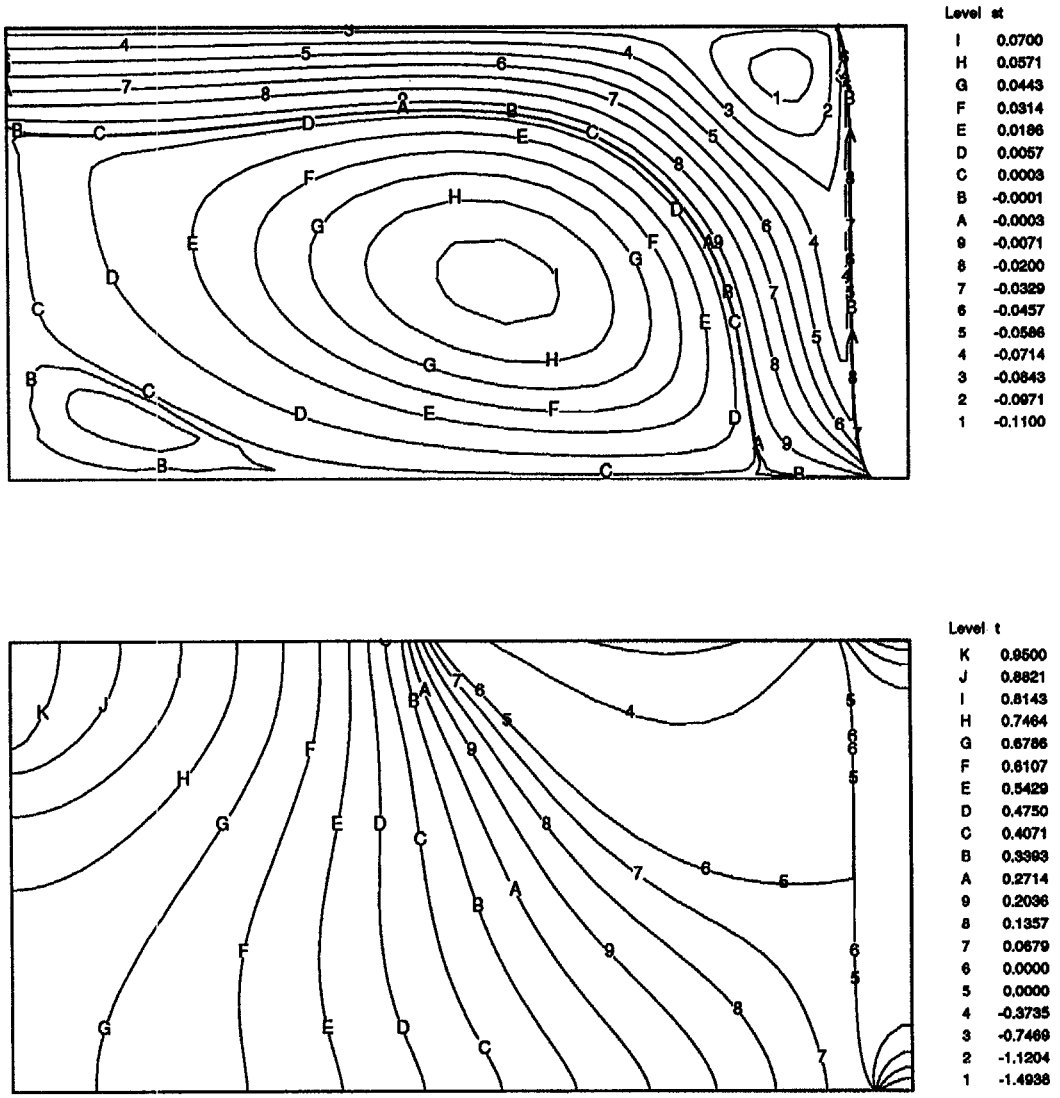

Fig. 12. Stream function distribution in the bath, and temperature contours in the solid and the melt, $q_s = 40$, $q_l = 4$.

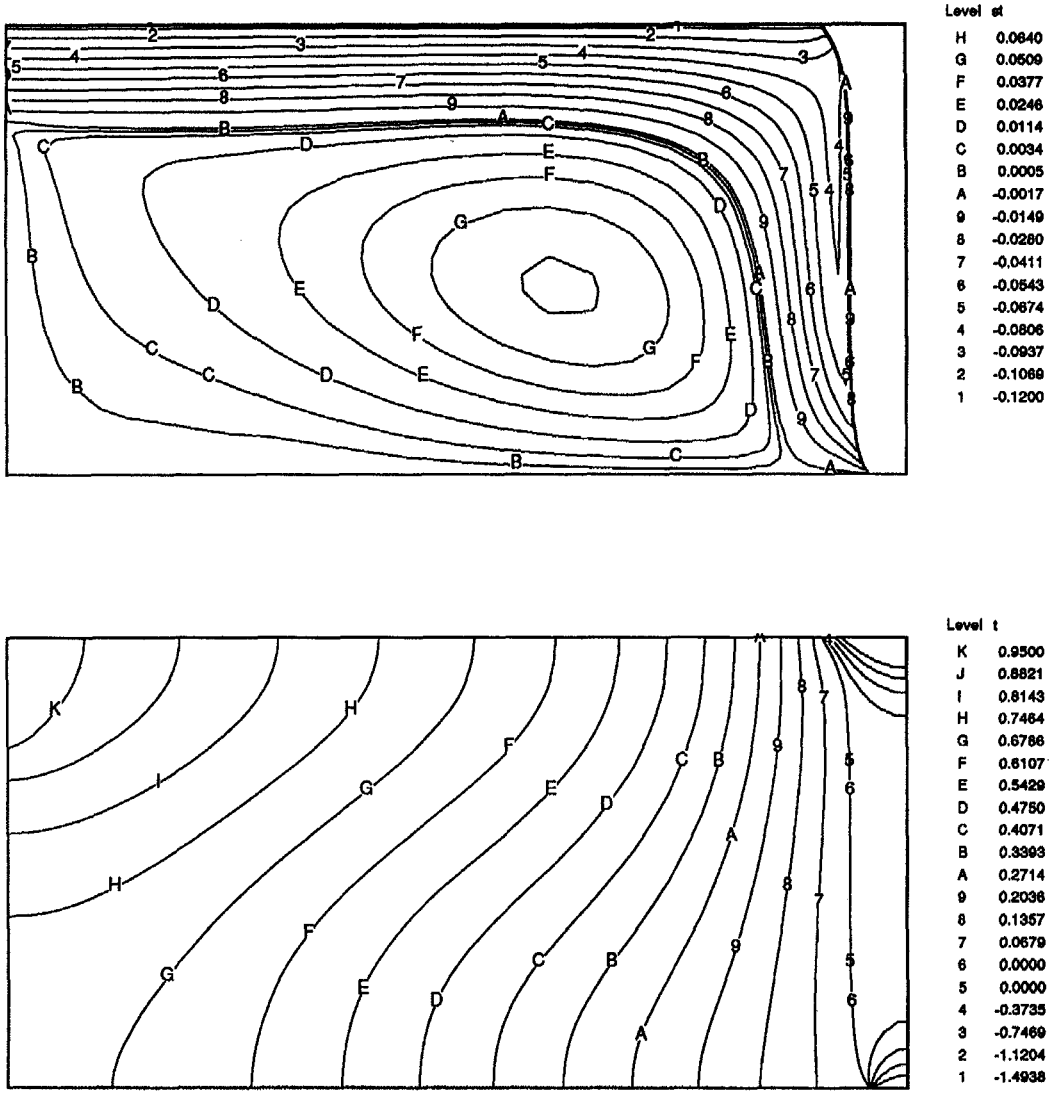

Fig. 13. Stream function distribution in the bath, and temperature contours in the solid and the melt, $q_s = 80$, $q_l = 0$.

solid and thermal buoyancy for the range of parameters examined. The effect of the surface tension on the solidification rate is very small, and its influence on the flow is limited to the meniscus region. The cooling of the solid emerging from the bath has a significant influence on the thickness of the solidified layer, while the cooling of the free surface causes a small change in the thickness by changing the flow field in the bath.

REFERENCES

1. D. C. Prior and D. E. Tonini, Hot dip galvanizing of high strength low alloy steel, *Metal Finishing* **82,** 15–19 (1984).
2. T. H. Cook, D. E. Mergen and D. L. Clark, Increasing profits in hot dip galvanizing, *Metal Finishing* **84,** 23–27 (1986).
3. P. P. Harrmann and D. Wildmann, Fabrication of planar dielectric waveguide with high optical damage threshold, *J. Quantum Electron.* **19,** 1735–1737 (1983).
4. D. W. Hewak and J. W. Y. Lit, Fabrication of tapers and lenslike waveguides by a microcontrolled dip coating procedure, *Appl. Opt.* **27,** 4562–4564 (1988).
5. C. S. Townsend and W. C. Bilski, Closed loop control of coating weight on a hot dip galvanizing line, *Iron Steel Engnr* **65,** 44–47 (1988).
6. R. V. Seeniraj and T. K. Bose, Freeze-coating on a continuous moving sheet and on an axially moving cylinder, *Warme Stoffubertragung* **15,** 239–243 (1981).
7. F. B. Cheung, Analysis of freeze coating on a non-isothermal moving plate by a perturbation method, *J. Heat Transfer* **107,** 549–556 (1985).
8. H. Zhang, M. K. Moallemi and S. Kumar, Analytical and numerical modeling of the dip-coating process, *J. Heat Transfer* **115,** 453–460 (1993).
9. S. B. Agarwal and R. A. Legault, An analysis of significance of coating thickness on the corrosion behavior of hot dip aluminized steel, *NACE J. Mater. Perform.* **16,** 19–23 (1983).

10. J. A. Thornton and H. F. Graff, An analytical description of the jet finishing process for hot-dip metallic coatings on strip, *Metall. Trans. B* **7,** 607–618 (1976).
11. M. K. Moallemi and H. Zhang, Surface tension effects on solidification of thin films via dip coating process, *J. Mater. Process. Manuf. Sci.* **2,** 233–243 (1993).
12. M. N. Ozisik, *Heat Conduction*. Wiley, New York (1980).
13. F. M. White, *Viscous Fluid Flow* (2nd Edn), pp. 50–91. McGraw-Hill, New York (1991).
14. H. Zhang and M. K. Moallemi, MAGG—a multizone adaptive grid generation technique for simulation of moving and free boundary problems, *Numer. Heat Mass Transfer* (to appear).
15. H. Zhang, A multizone adaptive grid generation technique for simulations of moving and free boundary problems, Ph.D. Thesis, Polytechnic University, Brooklyn, NY (1993).
16. J. U. Brackbill and J. S. Saltzman, Adaptive zoning for singular problems in two dimensions, *J. Comput. Phys.* **46,** 342–368 (1982).
17. J. F. Thomson, Z. U. Warsi and C. W. Mastin, *Numerical Grid Generation—Foundations and Applications*. North-Holland, Amsterdam (1985).
18. J. F. Thompson, A general three-dimensional elliptic grid generation system on a composite block structure, *Computer Meth. Appl. Mech. Engng* **64,** 377–411 (1987).
19. H. J. Kim and J. F. Thompson, Three-dimensional adaptive grid generation on a composite-block grid, *AIAA J.* **28,** 470–477 (1990).
20. Z. U. A. Warsi and J. F. Thompson, Application of variational methods in the fixed and adaptive grid generation, *Computers Math. Applic.* **19,** 31–41 (1990).
21. B. S. Gottfried and J. Weisman, *Introduction to Optimization Theory*. Prentice-Hall, NJ (1973).
22. H. Akima, A new method of interpolation and smooth curve fitting based on local procedures, *J. Assoc. Comput. Machin.* **17,** 589–602 (1970).
23. K. C. Karki and S. V. Patankar, Calculation procedure for viscous incompressible flows in complex geometries, *Numer. Heat Transfer* **14,** 295–307 (1988).
24. C. J. Kim and M. Kaviany, A numerical method for phase-change problems with convection and diffusion, *Int. J. Heat Mass Tranfer* **35,** 457–467 (1992).